Supporting Information

1 Supplementary methods

1.1 Conductivity effective mass

The conductivity effective mass (m^*) was determined based on Boltzmann transport theory[1,2] and is defined as[3]:

$$\frac{1}{m^*_{\alpha\beta}(T;\mu)} = \frac{\sigma_{\alpha\beta}(T;\mu)}{e^2\tau} \times \frac{1}{n(T;\mu)} \tag{1}$$

Where α and β denote Cartesian coordinates, T is the temperature, μ is the chemical potential, σ is the conductivity, e is the electron charge, τ is the relaxation time and n is the carrier concentration. τ was assumed to be a constant at all k-points and all bands, and was set to 10^{-14} s in this work. The conductivity tensor $\sigma_{\alpha\beta}$ is related to the electronic band structures by[4]:

$$\sigma_{\alpha\beta} = -e^2 \sum_n \int \frac{\mathrm{d}\mathbf{k}}{8\pi^3} \frac{\partial f^0_{n\mathbf{k}}}{\partial \varepsilon_{n\mathbf{k}}} v_{n\mathbf{k},\alpha} v_{n\mathbf{k},\beta} \tau_{n\mathbf{k}} \tag{2}$$

Where $\varepsilon_{n\mathbf{k}}$ is the energy of the nth band at the wave vector $\mathbf{k}$, v is the group velocity. The Fermi-Dirac distribution $f^0_{n\mathbf{k}}$ is given by:

$$f^0_{n\mathbf{k}} = \frac{1}{\exp[(\varepsilon_{n\mathbf{k}} - \varepsilon_F)/k_B T] + 1} \tag{3}$$

Where ε_F is the Fermi level and k_B is the Boltzmann constant.

According to the above equations, the conductivity effective mass depends on the position of ε_F (controlled by n) and T. In this work, T was set to 300 K. The conductivity effective mass then depends on n in that it controls the states over which v^2 is averaged. By setting n to 10^{13} cm^{-3} in this work, we therefore sample states close to the conduction and valence band edges that will control transport.

1.2 Optical absorption coefficients

The optical absorption coefficients (α) were calculated from the dielectric function using the equation:

$$\alpha(\omega) = \frac{4\pi}{\lambda} k(\omega) \tag{4}$$

Where ω and λ are the frequency and wavelength of the incident light, respectively. $k(\omega)$ is the extinction coefficient defined as

$$k(\omega) = \sqrt{\frac{\sqrt{\varepsilon_1^2 + \varepsilon_2^2} - \varepsilon_1}{2}} \tag{5}$$

Where ε_1 and ε_2 are the real and imaginary parts of the high-frequency dielectric constants, respectively.

1.3 Radiative limit of solar conversion efficiency

The photon absorptivity a at the energy E is defined as:

$$a(E; W) = 1 - \exp(-2\alpha(E)W) \tag{6}$$

Where W is the film thickness and α is the optical absorption coefficients. When $W \to \infty$, a approaches 1.

Under the assumption that one absorbed photon generates exactly one electron-hole pair, the short-circuit current J_{SC} is given by:

$$J_{\mathrm{SC}}(W) = e \int_0^{\infty} a(E; W)\Phi_{\mathrm{sun}}(E)\mathrm{d}E \tag{7}$$

Where e is the elementary charge, $\Phi_{\mathrm{sun}}(E)$ is solar photon flux density at the photon energy E.

The radiative recombination rate R_{rad} at temperature T and voltage V is given by:

$$R_{\mathrm{rad}}(V) = \frac{2\pi}{c^2 h^3} \int_0^{\infty} a(E; W)[e^{E - eV/k_B T} - 1]^{-1} E^2 \mathrm{d}E \tag{8}$$

The net current density J^{rad} limited by radiative recombination is given by:

$$J^{\mathrm{rad}}(V; W) = J_{\mathrm{SC}}(W) + J_0^{\mathrm{rad}}(W)(1 - e^{\frac{eV}{k_{\mathrm{B}}T}}) \tag{9}$$

Where the saturation current $J_0^{\mathrm{rad}} = eR_{\mathrm{rad}}(0)$.

The maximum efficiency is defined as the ratio of the maximum power density to the incident light power density, and the radiative limit of conversion efficiency is given by:

$$\eta_{max} = \max_V\left(\frac{J^{\mathrm{rad}}V}{e\int_0^{\infty} E\Phi_{\mathrm{sun}}(E)\mathrm{d}E}\right) \tag{10}$$

2 Binding energies

The substructures for calculating the inter-ribbon binding energies (E_b) are shown in Fig. S1. Fig. S1a is the 1D $[\mathrm{Sb_4X_6}]_n$ ribbon in isolation and Fig. S1b is the 2D ribbon periodically repeated along a and b directions. Table S1 shows E_b calculated by PBE and HSE06 functionals without vdW corrections. Compared with the results obtained by the HSE06 functional and D3 dispersion correction (shown in Table 2), the E_b here are much lower especially along the c direction, which is attributed to larger lattice parameters in the c direction without vdW corrections. This indicates that the inclusion of vdW corrections is necessary to reproduce the crystal structures of $\mathrm{Sb_2X_3}$.

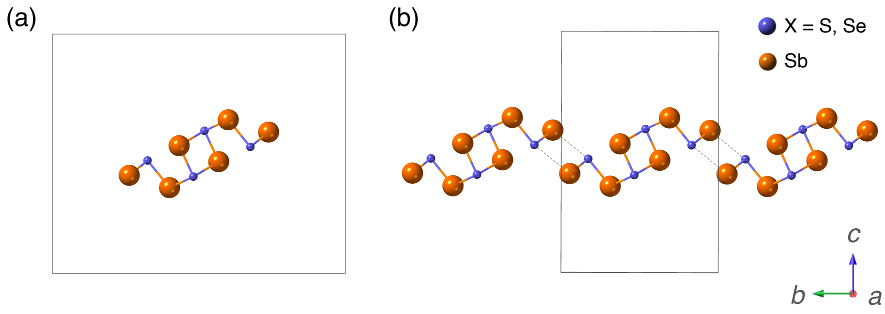

Figure S1: (a) 1D and (b) 2D substructures of $\mathrm{Sb_2X_3}$ used to calculate binding energies. The unit cells are represented by rectangles.

Table S1: Inter-ribbon binding energies ($\mathrm{kJ{\cdot}mol^{-1}}$) of $\mathrm{Sb_2S_3}$ and $\mathrm{Sb_2Se_3}$ without vdW corrections

System	Functional	$E_{\mathrm{b(b)}}$	$E_{\mathrm{b(c)}}$	
		per bond	per bond (N=16)	per atom (N=20)
$\mathrm{Sb_2S_3}$	PBE	19.66	4.32	3.46
	HSE06	13.77	3.81	3.05
$\mathrm{Sb_2Se_3}$	PBE	23.68	3.93	3.14
	HSE06	14.87	3.93	3.14

3 Electronic band structures

Calculated electronic band structures are shown in Fig. S2. According to our results, $\mathrm{Sb_2S_3}$ and $\mathrm{Sb_2Se_3}$ are indirect semiconductors with indirect (direct) band gaps of 1.79 (1.95) and 1.42 (1.48) eV, respectively, which are in reasonable agreement with previous experimental[5–12] and theoretical studies[13–18].

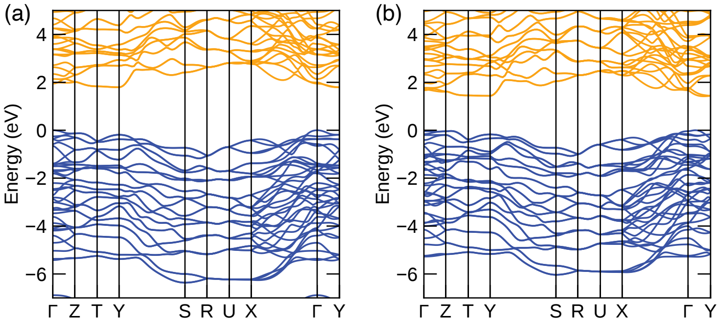

Figure S2: Electronic band structures of (a) Sb_2S_3 and (b) Sb_2Se_3.

4 Fermi surfaces

Electron Fermi surfaces (0.08 and 0.12 eV above the CBM) and hole Fermi surfaces (0.08 and 0.12 eV below the VBM) of Sb_2S_3 and Sb_2Se_3 are shown in Fig. S3 and S4, respectively. The shapes are qualitatively consistent with the results obtained by 0.10 eV above (below) the CBM (VBM), indicating our conclusions are robust.

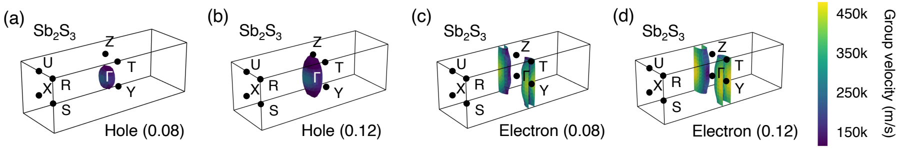

Figure S3: Fermi surfaces of Sb_2S_3. (a) and (b) are hole Fermi surfaces (0.08 and 0.12 eV below the VBM, respectively), while (c) and (d) are electron Fermi surfaces (0.08 and 0.12 eV above the CBM, respectively). The different colors represent the magnitude of group velocity (m/s)

5 Convergence tests

5.1 Total energies

Convergence tests of total energies with respect to k-point density were performed using the optB86b-vdW functional with a plane-wave energy cutoff of 400 eV. As shown in Table S2, total energies of Sb_2S_3 and Sb_2Se_3 converge to within 1 meV/atom at a k-point mesh of 7×2×2.

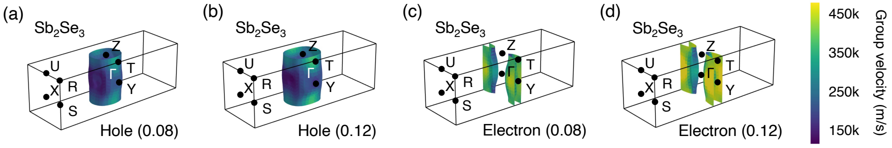

Figure S4: Fermi surfaces of Sb_2Se_3. (a) and (b) are hole Fermi surfaces (0.08 and 0.12 eV below the VBM, respectively), while (c) and (d) are electron Fermi surfaces (0.08 and 0.12 eV above the CBM, respectively). The different colors represent the magnitude of group velocity (m/s)

Table S2: Total energies (eV) per unit cell of Sb_2S_3 and Sb_2Se_3 with respect to *k*-point density

System	*k*-point grid	Total energy
Sb_2S_3	7×2×2	-56.164
	10×3×3	-56.167
	14×4×4	-56.168
Sb_2Se_3	7×2×2	-47.126
	10×3×3	-47.131
	14×4×4	-47.132

5.2 Effective masses

The convergence of effective masses were performed using the HSE06 functional and D3 dipersion correction as shown in Table S3. The results are sensitive to *k*-point mesh especially along the z direction as a result of the non-parabolicity. A *k*-point mesh of 19×10×10 was used for calculations of effective masses in Sb_2S_3 and Sb_2Se_3.

Table S3: Effective masses of Sb_2X_3 with respect to k-point meshes. Values larger than 2 are rounded to the nearest whole numbers. The harmonic mean is represented by $\overline{m}^*$.

System	k-point grid	x		y		z		$\overline{m}^*$	
		m_e^*/m_0	m_h^*/m_0	m_e^*/m_0	m_h^*/m_0	m_e^*/m_0	m_h^*/m_0	m_e^*/m_0	m_h^*/m_0
Sb_2S_3	14×4×4	0.12	0.39	1.18	0.67	7	1.17	0.32	0.61
	15×6×6	0.16	0.42	1.10	0.67	5	0.62	0.41	0.55
	16×7×7	0.17	0.42	1.25	0.66	6	0.98	0.44	0.61
	17×8×8	0.18	0.45	1.04	0.66	5	0.97	0.45	0.63
	18×9×9	0.16	0.46	1.09	0.65	6	0.97	0.41	0.63
	19×10×10	0.16	0.47	0.92	0.65	5	0.97	0.40	0.64
Sb_2Se_3	14×4×4	0.11	0.89	0.86	0.73	7	3	0.29	1.06
	15×6×6	0.12	0.87	0.79	0.57	5	3	0.31	0.93
	16×7×7	0.13	0.90	0.98	0.56	7	5	0.34	0.97
	17×8×8	0.14	0.94	0.84	0.52	6	4	0.35	0.93
	18×9×9	0.14	0.89	1.00	0.53	8	5	0.36	0.93
	19×10×10	0.14	0.85	0.81	0.55	7	3	0.35	0.90

5.3 Dielectric constants

The convergence of high-frequency dielectric constants (ε_∞) is usually sensitive to k-point density and number of bands, while the convergence of ionic dielectric constants ($\varepsilon_{\text{ionic}}$) is always related to k-point density and plane-wave energy cutoff[19,20]. Convergence tests of dielectric constants (shown in Table S4 and S5) were performed using the optB86b-vdW functional. High-frequency dielectric constants converge to ∼0.1 when the number of bands is 128 and k-point meshes are 12×4×4 (15×6×6) for Sb_2S_3 (Sb_2Se_3). The results of high-frequency dielectric constants in the main text were obtained by the HSE06 functional and D3 correction using the converged parameters shown above. Ionic dielectric constants converge to within 0.1 when the plane-wave energy cutoff is 700 (600) and k-point mesh is 15×6×6 (16×7×7) for Sb_2S_3 (Sb_2Se_3), which are the settings used for our results.

Table S6 shows vibrational frequencies extracted from DFPT phonon calculations at the Γ point which are used for calculating ionic contribution to dielectric constants. There are 3 acoustic phonon modes and 57 optical phonon modes with no imaginary phonon modes, indicating our calculations are solid.

For optical absorption coefficients calculations, k-point mesh was set to 15×6×6 and the number of bands was set to 160, as the optical absorption coefficients were calculated from high-frequency dielectric constants and they will show the same convergence behaviour. The optical absorption coefficients were calculated using tetrahedron method with Blöchl corrections.

Table S4: High-frequency dielectric constants (ε_∞) of Sb_2X_3 with respect to number of bands and k-point meshes

System	Number of bands	k-point grid	ε_∞			Difference		
			x	y	z	x	y	z
Sb_2S_3	128	6×2×2	16.79	17.33	13.07			
		10×3×3	17.66	17.29	12.89	-0.87	0.05	0.18
		12×4×4	17.57	17.24	12.87	0.08	0.05	0.02
		15×6×6	17.60	17.27	12.89	-0.03	-0.03	-0.02
	68	12×4×4	15.18	14.87	9.93			
	88		17.08	16.70	12.28	-1.90	-1.83	-2.36
	108		17.48	17.13	12.76	-0.40	-0.43	-0.48
	128		17.57	17.24	12.87	-0.09	-0.11	-0.11
	148		17.61	17.27	12.91	-0.04	-0.04	-0.03
Sb_2Se_3	128	6×2×2	22.29	26.17	18.00			
		10×3×3	24.30	25.86	17.58	-2.00	0.31	0.31
		12×4×4	24.08	25.94	17.57	0.22	-0.08	-0.08
		15×6×6	24.12	25.99	17.60	-0.05	-0.05	-0.05
	68	15×6×6	21.70	23.57	14.40			
	88		23.64	25.47	17.04	-1.94	-1.89	-2.65
	108		24.04	25.89	17.50	-0.39	-0.42	-0.46
	128		24.13	25.99	17.60	-0.09	-0.11	-0.10
	148		24.17	26.02	17.64	0.04	-0.03	-0.04

Table S5: Ionic dielectric constants ($\varepsilon_{\mathrm{ionic}}$) of Sb_2X_3 with respect to plane-wave energy cutoffs and k-point meshes

System	Energy cutoff	k-point grid	ε_∞			Difference		
			x	y	z	x	y	z
Sb_2S_3	600	12×4×4	87.42	83.33	4.89			
		15×6×6	87.36	83.26	4.89	0.06	0.07	0.00
		16×7×7	87.34	83.22	4.89	0.02	0.04	0.00
	400	15×6×6	87.41	82.86	4.88			
	500		87.42	83.10	4.88	-0.01	-0.24	0.00
	600		87.36	83.26	4.89	0.06	-0.16	-0.01
	700		87.39	83.24	4.89	-0.03	0.02	0.00
Sb_2Se_3	600	12×4×4	70.68	113.64	4.47			
		15×6×6	70.53	113.32	4.47	0.15	0.32	0.00
		16×7×7	70.53	113.26	4.47	0.00	0.06	0.00
	400	15×6×6	70.54	112.98	4.47			
	500		70.53	113.25	4.47	0.01	-0.28	0.00
	600		70.53	113.32	4.47	0.00	-0.07	0.00

Table S6: Vibrational frequencies (THz) of Sb_2X_3 at the Γ point

Normal mode	Vibrational frequency		Normal mode	Vibrational frequency	
	Sb_2S_3	Sb_2Se_3		Sb_2S_3	Sb_2Se_3
1	6.38	9.67	31	3.19	4.84
2	6.19	9.19	32	3.16	4.84
3	5.95	8.88	33	2.94	3.90
4	5.93	8.82	34	2.86	3.83
5	5.82	8.80	35	2.79	3.78
6	5.75	8.74	36	2.72	3.71
7	5.62	8.52	37	2.68	3.59
8	5.33	8.34	38	2.58	3.43
9	5.28	8.32	39	2.44	3.33
10	5.21	7.86	40	2.27	2.98
11	5.15	7.60	41	2.14	2.81
12	5.13	7.50	42	1.90	2.52
13	4.99	7.47	43	1.88	2.35
14	4.90	7.44	44	1.79	2.20
15	4.61	7.28	45	1.70	2.19
16	4.44	7.19	46	1.69	2.00
17	4.25	6.79	47	1.65	1.90
18	4.22	6.73	48	1.61	1.89
19	4.21	6.49	49	1.58	1.70
20	4.14	6.42	50	1.57	1.66
21	3.87	6.11	51	1.38	1.54
22	3.86	6.03	52	1.34	1.47
23	3.81	6.03	53	1.31	1.39
24	3.81	5.98	54	1.23	1.35
25	3.71	5.97	55	1.18	1.27
26	3.69	5.82	56	0.86	1.03
27	3.52	5.69	57	0.52	0.75
28	3.49	5.62	58	0	0
29	3.34	5.61	59	0	0
30	3.31	5.39	60	0	0

References

[1] N. W. Ashcroft, N. D. Mermin *et al.*, *Solid State Physics*, 1976.

[2] G. K. Madsen and D. J. Singh, *Comput. Phys. Commun.*, 2006, **175**, 67–71.

[3] Z. M. Gibbs, F. Ricci, G. Li, H. Zhu, K. Persson, G. Ceder, G. Hautier, A. Jain and G. J. Snyder, *NPJ Comput. Mater.*, 2017, **3**, 1–7.

[4] A. M. Ganose, J. Park, A. Faghaninia, R. Woods-Robinson, K. A. Persson and A. Jain, *Nat. Commun.*, 2021, **12**, 1–9.

[5] N. Yesugade, C. Lokhande and C. Bhosale, *Thin Solid Films*, 1995, **263**, 145–149.

[6] I. El Zawawi, A. Abdel-Moez, F. Terra and M. Mounir, *Thin Solid Films*, 1998, **324**, 300–304.

[7] M. Y. Versavel and J. A. Haber, *Thin Solid Films*, 2007, **515**, 7171–7176.

[8] M. Liu, Y. Gong, Z. Li, M. Dou and F. Wang, *Appl. Surf. Sci.*, 2016, **387**, 790–795.

[9] A. Torane, K. Rajpure and C. Bhosale, *Mater. Chem. Phys.*, 1999, **61**, 219–222.

[10] S. Messina, M. Nair and P. Nair, *J. Electrochem. Soc.*, 2009, **156**, H327.

[11] Y. Lai, Z. Chen, C. Han, L. Jiang, F. Liu, J. Li and Y. Liu, *Appl. Surf. Sci.*, 2012, **261**, 510–514.

[12] C. Chen, W. Li, Y. Zhou, C. Chen, M. Luo, X. Liu, K. Zeng, B. Yang, C. Zhang, J. Han *et al.*, *Appl. Phys. Lett.*, 2015, **107**, 043905.

[13] R. Vadapoo, S. Krishnan, H. Yilmaz and C. Marin, *Nanotechnology*, 2011, **22**, 175705.

[14] R. Vadapoo, S. Krishnan, H. Yilmaz and C. Marin, *Phys. Status Solidi B*, 2011, **248**, 700–705.

[15] R. Caracas and X. Gonze, *Phys. Chem. Miner.*, 2005, **32**, 295–300.

[16] T. B. Nasr, H. Maghraoui-Meherzi, H. B. Abdallah and R. Bennaceur, *Physica B Condens. Matter.*, 2011, **406**, 287–292.

[17] H. Koç, A. M. Mamedov, E. Deligoz and H. Ozisik, *Solid State Sci.*, 2012, **14**, 1211–1220.

[18] C. N. Savory and D. O. Scanlon, *J. Mater. Chem. A*, 2019, **7**, 10739–10744.

[19] M. S. Hybertsen and S. G. Louie, *Phys. Rev. B*, 1987, **35**, 5585.

[20] V. Olevano, M. Palummo, G. Onida and R. Del Sole, *Phys. Rev. B*, 1999, **60**, 14224.